

Disentangling the Role of Forest Structure and Functional Traits for the Thermal Balance in the Mediterranean-Temperate Ecotone

Adria Barbeta¹, Diego G. Miralles², Teresa E. Gimeno³, Leire Mendiola⁴, Santiago Sabaté¹, and Jofre Carnicer⁵

¹Universitat de Barcelona

²Ghent University

³Basque Center for Climate Change (BC3)

⁴Basque Centre for Climate Change (BC3)

⁵CREAF

April 7, 2023

1 **Disentangling the Role of Forest Structure and Functional Traits in the Thermal**
2 **Balance of the Mediterranean–Temperate Ecotone**

3 **A. Barbeta^{1*}, D. G. Miralles², L. Mendiola^{3,4}, T. E. Gimeno^{3,5}, S. Sabaté^{1,5} and J. Carnicer^{1,5}**

4 1. BEECA-UB, Department of Evolutionary Biology, Ecology and Environmental Sciences,
5 University of Barcelona, Barcelona, Catalonia, Spain. 2. Hydro-Climate Extremes Lab (H-CEL),
6 Ghent University, Ghent, Belgium. 3. Basque Centre for Climate Change (BC3), Leioa, Spain. 4.
7 Errez Koop. Elk. Txikia, Aramaio, Araba. 5. CREAM, 08193 Bellaterra (Cerdanyola del Vallès),
8 Catalonia, Spain.

9 Corresponding author: Adrià Barbeta (adria.barbeta.margarit@gmail.com)

10 Address: Edifici Margalef, Avinguda Diagonal, 643, 08028 Barcelona, Catalonia, Spain.

11 **Key Points:**

- 12 • The thermal balance of forests is estimated at the plot-scale using ECOSTRESS-derived
13 canopy temperatures.
- 14 • Hot spells are mostly driven by advection rather than by land–atmosphere feedbacks.
- 15 • Forest structure and species-specific differences in plant water use correlate with heat
16 dissipation mechanisms.

17
18

19 Abstract

20 The thermal balance of forests is the result of complex land–atmosphere interactions. Different
21 climate regimes and plant functional types can have contrasting energy budgets, but little is known
22 about the influence of forest structure and functional traits. Here, we combined spaceborne
23 measurements of surface temperature from ECOSTRESS with ground-based meteorological data
24 to estimate the thermal balance at the surface ($\Delta T_{can-air}$) during four summers (2018–2021), at
25 the Mediterranean–temperate ecotone in the NE Iberian Peninsula. We analyzed the
26 spatiotemporal drivers of $\Delta T_{can-air}$ by quantifying the effects of meteorology, forest structure
27 (stand density, tree height) and ecophysiology (hydraulic traits), during normal days and hot spells.
28 Canopy temperatures (T_{can}) fluctuated according to changes in air temperature (T_{air}) but were on
29 average 4.2 K warmer. During hot spells, $\Delta T_{can-air}$ was smaller than during normal periods. We
30 attribute this decrease to the advection of hot and dry air masses from the Saharan region resulting
31 in a sudden increase in T_{air} relative to T_{can} . Vapor pressure deficit (VPD) was negatively
32 correlated with $\Delta T_{can-air}$, since the highest VPD values coincided with peaks in heat advection.
33 Nonetheless, T_{can} increased with VPD due to decreased transpiration (following stomatal closure),
34 even though sufficient soil water availability enabled some degree of evaporative cooling. Our
35 findings demonstrate that plot-scale forest structural and hydraulic traits are key determinants for
36 the forest thermal balance. The integration of functional traits and forest structure over relevant
37 spatial scales would improve our ability to understand and model land–atmosphere feedbacks in
38 forested regions.

39

40 Plain Language Summary

41 Forests exchange energy with the atmosphere. Different types of forests may result in substantially
42 different energy exchanges, but it is not clear which are the ecological factors causing these
43 differences. This is relevant because during hot spells, the way by which the surface dissipates
44 heat can either intensify or mitigate the air temperature increase. Here, we assessed how canopies
45 exchange heat with the atmosphere depending on the characteristics of the forest cover, in a region
46 densely covered by forests, with great ecological and climatic diversity, in the transition zone
47 between the Mediterranean and the temperate ecotone. We show that recent hot spells were not
48 aggravated by tree energy dissipation into the atmosphere. Instead, we argue that incoming hot air
49 masses, often travelling from northern Africa, reduced the exchange of energy between the surface
50 and the atmosphere, and so, the warming from below was not critical for the aggravation of these
51 hot spells. Yet, we found that there was high variability in the thermal balance of forests along the
52 ecoclimatic gradients of the study region that could not be explained by broad forest type
53 classifications. Instead, differences in the thermal balance and its influence on air temperature were
54 better explained by forests functional and structural characteristics, such as tree height or
55 functional type of the dominant species.

56 1 Introduction

57 Biological and physical properties of the Earth's surface regulate the exchange of energy
58 and matter with the atmosphere, by determining the rates and magnitudes of the surface water and
59 energy fluxes (Pitman, 2003). Processes such as evaporation, turbulent sensible heat transfer or
60 the upwelling of shortwave and longwave radiation modulate the local, regional and global

61 climate, and strongly vary as a function of the characteristics of the land cover (Bagley et al., 2017;
62 de Oliveira et al., 2019; Yan et al., 2014). The effects of surface structure on land–atmosphere
63 exchanges, and in turn on local climate, are often well understood; for example, the surface
64 properties of cities contribute to the development of urban heat islands, which can be mitigated by
65 increasing vegetation cover (Shiflett et al., 2017). Yet, land surface influences exceed local scales,
66 modulating for instance downwind precipitation patterns (Drumond et al., 2014; Keune &
67 Miralles, 2019; O’Connor et al., 2021; te Wierik et al., 2021). At the regional scale, the onset of
68 extreme temperature episodes is also influenced by a combination of atmospheric dynamics and
69 land–atmosphere feedbacks. There is evidence of direct causal associations between the
70 anomalous heat accumulation in the atmosphere and the preceding low soil moisture, which limits
71 the magnitude of latent heat fluxes over hundreds of square kilometers (Fischer et al., 2007;
72 Miralles et al., 2014, 2019). In addition to the short-term coupling dynamics between land and
73 atmosphere, the impacts of this coupling can reflect over longer timescales (Koster et al., 2004).
74 In fact, changes in land surface biological and physical properties occurring over decadal to
75 centurial scales may have long-lasting global impacts. For instance, the Earth’s greening caused
76 by the fertilization effect of anthropogenic CO₂ (e.g., Zhu et al., 2016; Zhang et al 2012) may have
77 partially mitigated global warming in recent decades through an increase in evaporative cooling
78 (Forzieri et al., 2017). The interest on the topic of land influence on climate has grown steadily in
79 recent years because of its important implications for future climate (Canadell et al., 2021; IPCC,
80 2021, p. 20; Seneviratne et al., 2021).

81 Land vegetation affects land–atmosphere energy, momentum and mass exchanges
82 (Anderegg et al., 2019; Ellison et al., 2017). The characteristics of vegetation regulate how much
83 solar radiation is reflected (Cescatti et al., 2012), partitioned into latent and sensible heat fluxes
84 (Williams & Torn, 2015) or absorbed and temporally stored, thus yielding an increase in surface
85 temperature (Meier et al., 2019). The sole categorization of vegetation into plant functional types
86 (PFTs) – such as conifer/broadleaf forests or grasslands – can help explain changes in surface
87 energy partitioning due to intrinsic properties of these PFTs (Forzieri et al., 2020), such as their
88 leaf area index, which are associated with different ecosystem functions (Migliavacca et al., 2021;
89 Nemani et al., 1996). Besides structural traits, plant physiological traits can also influence the
90 energy balance at the ecosystem-level. For instance, recent studies found that land–atmosphere
91 feedbacks during drought are modulated by plant hydraulic traits and forest specific composition
92 (Anderegg et al., 2018, 2019). This is because evaporative response of forests will depend not only
93 on atmospheric conditions but also on the form and function of specific tree species, and the soil
94 and landscape features that determine access to water resources (Barbeta & Peñuelas, 2017). In
95 another example, Teuling et al., (2010) demonstrated contrasting temporal dynamics of surface
96 energy fluxes during heatwaves in grasslands, which depict a more opportunistic water-use
97 strategy, compared to forests, with a more conservative water use. Grasslands respond to heat with
98 a fast increase in transpiration that initially minimizes sensible heat fluxes, but as soil moisture is
99 depleted, sensible heat fluxes progressively increase. In contrast, the more conservative water-use
100 in forests, combined with their lower albedo, yields an initially stronger increase in sensible heat
101 fluxes; after a few days, however, forests prevent heatwave amplification due to the sustained
102 transpiration enabled by a usually deeper root system. This example shows that differences among
103 plant functional types are critical to understand how the land feeds back into the atmospheric state,
104 and particularly during the evolution of hot spells. A key trait driving the energy balance of the
105 vegetation is surface conductance, defined as the inverse of the resistance to water diffusion along
106 the soil–plant–atmosphere continuum (Wang et al., 2019). To date, the study of the biotic

107 determinants of surface conductance has been, typically restricted to the consideration of different
108 PFTs (Gerken et al., 2019; Teuling et al., 2010). However, there is evidence that the surface
109 conductance can drastically differ among different types of forest and plant species (Wang et al.,
110 2019).

111 Canopy temperature (T_{can}) is largely driven by incoming radiation, and it determines
112 sensible heat, water and carbon fluxes (Still et al., 2021). Deviations of T_{can} from air temperature
113 (T_{air}) are often associated with fluctuations in surface and aerodynamic resistance to the heat
114 transfer by conduction and convection (sensible heat flux) (Grace, 1988). Simultaneously, T_{can}
115 influences and is influenced by tree transpiration, which reduces the temperature of the leaves by
116 'evaporative cooling' (Javadian et al., 2022). The difference between T_{can} and T_{air} (i.e. $\Delta T_{can-air}$)
117 can be seen as the integrative result of all the components of the energy balance of the canopy.
118 From the biological point of view, the relationship between T_{can} and T_{air} can be an indicator of
119 plant water stress (Fauset et al., 2018; Moyano et al., 2018). From an atmospheric standpoint,
120 $\Delta T_{can-air}$ may reflect the influence of non-local controls on T_{air} (e.g., advection, entrainment,
121 subsidence, condensation). As such, estimating $\Delta T_{can-air}$ at high temporal and spatial resolutions
122 provides valuable insights into dynamic land-atmosphere feedbacks and how these are modulated
123 by plant water-use strategies (Anderegg et al., 2019; Wang et al., 2019). This approach can help
124 elucidate how biotic and abiotic determinants interact and affect the surface energy balance of
125 forests.

126 In recent years, there has been an increase in the spatial and temporal resolution of remote
127 sensing products measuring land surface temperature (LST) that may be used as a proxy for T_{can}
128 in vegetated regions. More specifically, the ECOSystem Spaceborne Thermal Radiometer
129 Experiment on Space Station (ECOSTRESS) launched in 2018 by the National Aeronautics and
130 Space Administration (NASA) provides LST at a spatial resolution of 70x70m, every 3–5 days
131 (Fisher et al., 2020) and with high accuracy (Hulley et al., 2022). Interestingly, this high spatial
132 resolution enables the coupling of remotely-sensed LST with plot-scale variations in forest
133 structure, environmental conditions or any other variable measured at the fine scale (Javadian et
134 al., 2022). It is thus possible to achieve more detailed, mechanistic-oriented analyses of the forest
135 thermal balance, beyond the comparison of the thermal balance between different vegetation types.

136 Here we leverage the availability of spatially-dense datasets on forest structure,
137 meteorological conditions and topography for an ecologically and climatically diverse area in the
138 Mediterranean-temperate ecotone to investigate $\Delta T_{can-air}$, and its drivers over the growing
139 season. Particularly, we hypothesize that (i) $\Delta T_{can-air}$ will be higher during hot spells than in
140 normal days due to reduced transpiration and evaporative cooling and that (ii) forests with a more
141 conservative water-use and occupying the warmer and drier areas will present a relatively higher
142 $\Delta T_{can-air}$ during hot spells due to reduced transpiration rates (see e.g., Teuling et al., (2010)). Low
143 water availability should be correlated with forest structural properties – such as lower LAI,
144 aboveground biomass and basal area – so we do not expect structural variables to explain
145 additional variability in $\Delta T_{can-air}$, beyond that explained by climatic gradients (mean
146 precipitation, temperature and radiation). On the other hand, we also hypothesize (iii) a strong
147 effect on $\Delta T_{can-air}$ of variables that are directly related to heat dissipation through their effect on
148 surface roughness (Muller et al., 2021). Specifically, we expect that larger canopy height, canopy
149 cover and stand density (all variables analyzed here) have independent (and negative) effects on
150 $\Delta T_{can-air}$. Finally, since low transpiration rates should lead to higher $\Delta T_{can-air}$, we also

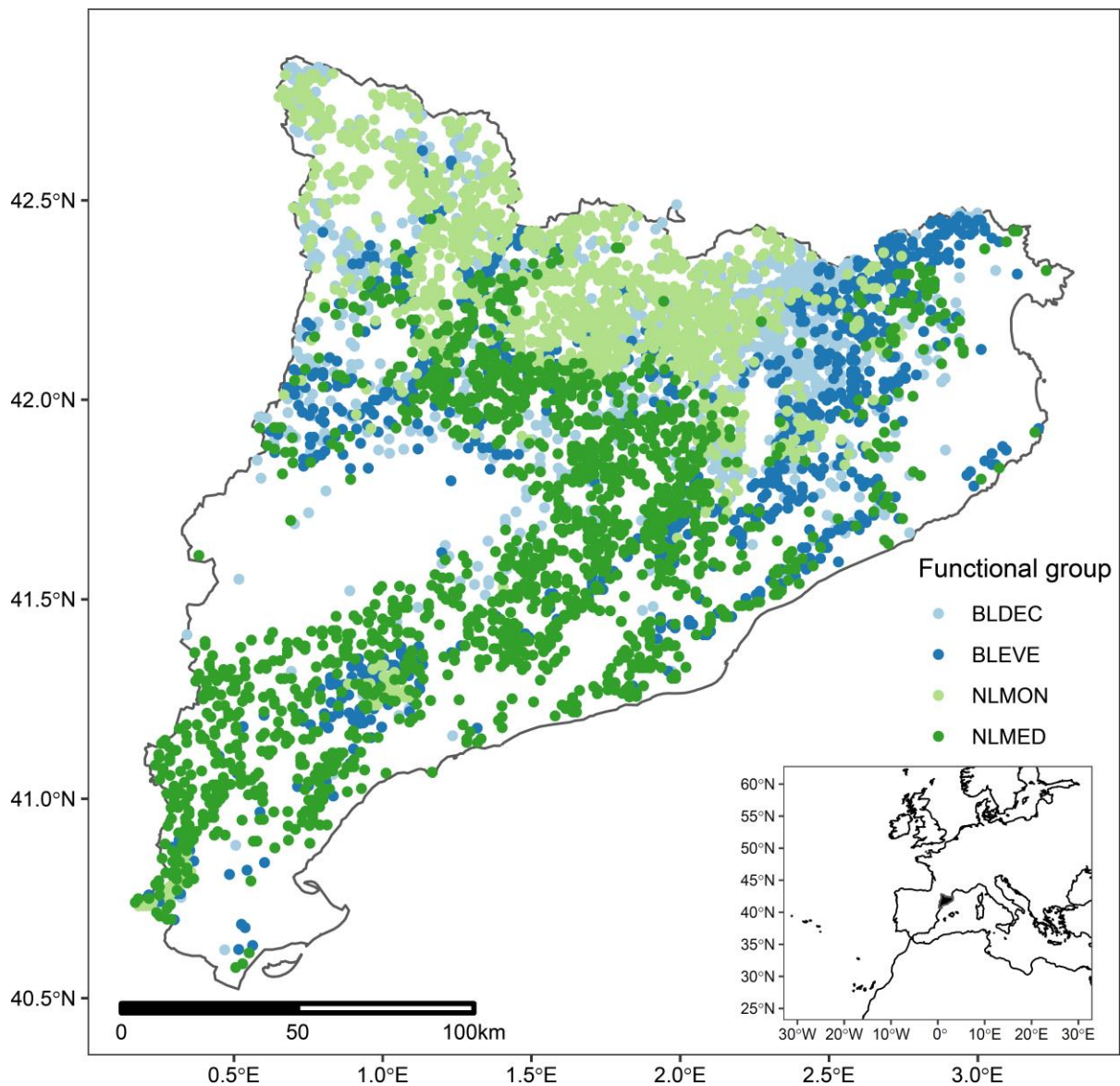
151 hypothesize that (iv) forests dominated by drought-resistant species (with a certain suite of
152 associated hydraulic traits) would show higher $\Delta T_{can-air}$, compared to those dominated by more
153 drought-sensitive species (Still et al., 2022). However, it would also be possible that some drought-
154 sensitive species with access to deep-water could maintain relatively high transpiration rates
155 during hot spells (Krich et al., 2022), and hence lower $\Delta T_{can-air}$.

156 **2 Data and Methods**

157 **2.1 Study Area**

158 The selected study area corresponds to Catalonia, an area covering 32114 km² in the NE of the
159 Iberian Peninsula, in the NW shores of the Mediterranean Sea. Catalonia is located at the transition
160 zone between Mediterranean and temperate climates, so its climate is predominantly
161 Mediterranean, but is also subjected to Atlantic, temperate and subtropical influences (Llebot,
162 2005). The complex orography in this area results into a high diversity in thermic regimes across
163 an altitude range from sea level to >3000 m a.s.l., as well as into drier/wetter areas due to
164 leeward/windward exposures relative to the Mediterranean sea, but also to the Atlantic Ocean
165 (Martín Vide, 2016). Hence, Catalonia depicts an unusually high climatic diversity for such a small
166 area, which ranges from cold semi-arid climates (BSk in the Köppen–Geiger classification) to
167 temperate ones (e.g., Cfa or Cfb in the same classification system), with coastal areas presenting a
168 typical hot-summer Mediterranean climate (Csa) (Beck et al., 2018). As such, mean annual
169 precipitation (MAP) ranges widely, from 350 to 1300 mm, with mean annual temperatures (MAT)
170 ranging from 0 to 17°C (Llebot, 2005). In line with the climatic diversity of the area, the relatively
171 high fraction of forested area – ca. 38% (Rosas et al., 2019) – is occupied by functionally and
172 structurally diverse forests, mostly dominated by tree species from the Fagaceae and Pinaceae
173 families (Roces-Díaz et al., 2018). The lowland forests in the coastal areas are dominated by
174 broadleaf evergreen tree species, such as *Quercus ilex* L., and needleleaf Mediterranean trees, such
175 as *Pinus halepensis* Mill., the latter occupying the drier coastal area and the inland lowland areas
176 (Fig. 1). Moister and cooler areas at mid altitudes (500–1600 m), and often with a maritime
177 influence, harbor forests dominated by broadleaf deciduous species, some common across Europe
178 (e.g., *Fagus sylvatica* L., *Fraxinus excelsior* L.), but also trees typical of the Mediterranean–
179 temperate biome transition (e.g., *Quercus pubescens* Willd., *Quercus faginea* Lam.). In the mid to
180 high altitudes of the Pyrenees, we find needleleaf montane forests dominated by coniferous species
181 that reach their southernmost distribution range in the study area, such as *Abies alba* Mill., *Pinus*

182 *uncinata* Ram. and *Pinus sylvestris* L. (Fig. 1). The diversity in forest structure, function and
 183 environmental conditions makes the area especially suitable for our research goals.



184

185 **Figure 1. Study area.** Map of Catalonia and the forest plots included in the analysis, with colored
 186 dots illustrating the functional group of the dominant species of each plot (light blue: BLDEC,
 187 broadleaf deciduous, dark blue: BLEVE, broadleaf evergreen, light green: NLMON, needleleaf

188 montane, dark green: NLMED, needleleaf Mediterranean). Inset: the black area represents the
189 location of the study area (Catalonia) within the Western Mediterranean Basin.

190 2.2 Forest Structural, Topographical and Meteorological Data and Species-Specific 191 Hydraulic Traits

192 The dataset comprises 4131 forest plots belonging to the Fourth Spanish Forest National
193 Inventory (IFN4) conducted between 2013–2016
194 ([https://www.miteco.gob.es/es/biodiversidad/temas/inventarios-nacionales/inventario-forestal-](https://www.miteco.gob.es/es/biodiversidad/temas/inventarios-nacionales/inventario-forestal-nacional/cuarto_inventario.aspx)
195 [nacional/cuarto_inventario.aspx](https://www.miteco.gob.es/es/biodiversidad/temas/inventarios-nacionales/inventario-forestal-nacional/cuarto_inventario.aspx)). From this inventory, we extracted data on forest stand
196 composition, i.e., the dominant species, according to measurements of basal area and the
197 percentage of basal area of the dominant species. A forest with more than 80% of basal area of the
198 same species was considered a pure stand; conversely, those stands in which the basal area of the
199 dominant species was below 80% were considered as mixed. From the IFN4, we also extracted
200 plot topographic information including the elevation, the aspect of the plot (North, South, East,
201 West or flat), the slope of the terrain (%) and the type of curvature, where positive values denote
202 a concave curvature (i.e., hills) and negative values denote a convex curvature (i.e., valleys).
203 Average climatic data for each plot was also available (see Table S1). Forest structural data was
204 extracted from each of the IFN4 plots from a LIDAR-based dataset with a 20x20m resolution
205 collected between 2008–2011 and processed by the Center of Ecological Research and Forest
206 Applications (CREAF) and the Catalan Geologic and Cartographic Institute (ICGC). The variables
207 included in our analysis were: total aerial biomass, foliar biomass, basal area, tree cover, diameter
208 at breast height (DBH), leaf area index, stand density and mean tree height (Table S2). In addition,
209 we used a dataset on tree hydraulics traits collected in the same forest plot network across aridity
210 gradients of the six most abundant species; a detailed description of the methods used to measure
211 the hydraulic traits is provided by Rosas et al. (2019). Because of the large number of dominant
212 species represented in our dataset (60, according to our dominance criteria based on basal area,
213 Barbeta et al. (2022)), for some of our analyses we grouped species in four functional groups:
214 needleleaf Mediterranean (NLMED), needleleaf montane (NLMON), broadleaf evergreen
215 (BLEVE) and broadleaf deciduous (BLDEC).

216 Meteorological data specific for the location of each plot and for the period 2018–2021 was
217 obtained using the R package *meteoland* (De Cáceres et al., 2018). This package provides estimates
218 of daily weather variables over the landscape by spatial interpolation of daily weather records, at
219 a resolution of 30x30 meters, and accounting for the effects of elevation, slope, and aspect. For the
220 present dataset, data from stations of the Spanish State Meteorology Agency (AEMET) and the
221 Catalan Meteorological Service (SMC) were used as input data. The meteorological data included
222 daily air temperature, relative humidity, wind speed, precipitation, potential evaporation and solar
223 radiation. With the interpolated variables we also calculated the climatic water balance (CWB) of
224 the 30 days prior to the remote sensing measurement (precipitation minus potential evaporation),
225 for each plot. After the spatial interpolation using *meteoland* (De Cáceres et al., 2018), midday
226 daily vapor pressure deficit (VPD) was estimated with the *rh.to.VPD* function from the R package
227 *bigleaf* (Knauer et al., 2018). Next, we downscaled these interpolated daily data on wind speed,
228 air temperature (T_{air} , at canopy height) and relative humidity to hourly scales, using hourly data
229 from the network of automatic meteorological stations XEMA
230 (<https://www.meteo.cat/observacions/xema>), so that each meteorological observation would be
231 more comparable to the overpass of ECOSTRESS. Air temperature at ground-level was

232 transformed into air temperature at canopy height, by using temperature scales in forested surfaces
233 (Bonan, 2015) – see Text S1 for further details.

234 Forest structural, topographical and meteorological data were accessed through the R package
235 *lfcdata* (<https://github.com/MalditoBarbudo/lfcdata>), which gives direct access to the data of the
236 Catalan Forest Laboratory (<https://laboratoriforestal.creaf.cat/>), an initiative of CREAM and the
237 Forest Science and Technology Center of Catalonia (CTFC). We also obtained shortwave albedo
238 data from MODIS MCD43A3 datasets that provide both black-sky and white-sky albedo. We used
239 only black-sky albedo (directional hemispherical reflectance) for the analysis, yet these values
240 were highly correlated with white-sky albedo ($R^2=0.96$). We calculated the average black-sky
241 albedo from June to September for each of the plots and the period of study.

242 2.3 Land Surface Temperature (LST) Data from ECOSTRESS

243 We retrieved LST data from the ECOSystem Spaceborne Thermal Radiometer Experiment on
244 Space Station (ECOSTRESS, <https://ecostress.jpl.nasa.gov/>), particularly, from the ECO2LSTE
245 Version 1, a Level-2 product from ECOTRESS. ECO2LSTE provides LST at a spatial resolution
246 of 70x70 m and every 3–5 days (Fisher et al., 2020). Our choice of ECOSTRESS over other
247 remotely-sensed LST products was based on the unique combination of high spatial resolution and
248 relatively more frequent observations. For each of the forest plots in our network, we downloaded
249 the LST for all dates available in the ECO2LSTE Version 1 collection through the Application for
250 Extracting and Exploring Analysis Ready Samples (AppEEARS) data portal. From that, we used
251 the product quality flags to select only those clear sky observations with the best quality and a LST
252 accuracy below 1.5 K. The period spanned from the beginning of the ECOSTRESS mission (2018)
253 to December 2021. Here, we only used data from June–September, comprising the growing season
254 in the study area. Finally, we selected only observations corresponding to the central hours of the
255 day (9–15 h UTC), during which the vegetation transpires and thus dynamically influences LST.

256 2.4 Data Processing

257 Daily meteorological data for each plot (wind speed, air temperature at canopy height and relative
258 humidity) were obtained by spatial interpolation (De Cáceres et al., 2018) (see section 2.3 for
259 further details) and maximum daily vapor pressure deficit (VPD) was estimated with the *rh.to.VPD*
260 function from the R package *bigleaf* (Knauer et al., 2018). Next, we downscaled these interpolated
261 daily data on wind speed, air temperature (T_{air} , at canopy height) and relative humidity to hourly
262 scales, using hourly data from the network of automatic meteorological stations XEMA
263 (<https://www.meteo.cat/observacions/xema>), so that each meteorological observation would be
264 more comparable to the overpass of ECOSTRESS. Once we had a complete database of air
265 temperature (T_{air}) collocated with their corresponding LST observation (T_{can} , from the
266 ECO2LSTE version 1 (see section 2.3), we calculated $\Delta T_{can-air}$, i.e., the difference (between
267 land (T_{can}) and air temperature (T_{air}). Positive values of $\Delta T_{can-air}$ indicate that the land surface
268 (i.e. the forest upper canopy) is warmer than the free air above it, whereas negative values indicate
269 that the land surface is cooler.

270 Our study period (June–September 2018–2021) was divided into normal periods and hot
271 spells. According to the Catalan Meteorological Service, hot spells are defined as periods in which
272 temperatures above the 98th percentile of June–August maximum temperatures (according to a 10-

273 year record) at any given *XEMA* meteorological station. Hot spells are considered a heatwave when
274 they last for 3 days or more. During the 2018–2021 study period, the area experienced five hot
275 spells.

276 2.5 Statistical Analysis

277 We first tested for the effect of several categorical variables on $\Delta T_{can-air}$ and T_{can} : (a)
278 functional group of the plot's dominant species, (b) stand composition (pure versus mixed stands).
279 We also assessed (c) differences between normal and hot spell days. For each of these fixed
280 categorical factors we fitted a generalized linear mixed model (GLMM) with hour of the
281 observation, aspect of the plot and the plot identifier as random factors, using the function *lmer* of
282 the R package *lme4* (Bates et al., 2015). The mean annual precipitation was also added to these
283 models to account for gradients in annual rainfall. We then checked for pairwise differences with
284 Tukey post-hoc tests from the R package *emmeans* (Lenth et al., 2018). Next, we tested for the
285 effects of continuous forest variables on $\Delta T_{can-air}$ and T_{can} . We initially considered the
286 correlation with 19 variables characterizing forest structure (basal area, stand density, tree cover,
287 total aerial biomass, DBH, mean tree height, foliar biomass, LAI, and albedo), topography (slope,
288 curvature and distance to the sea), meteorology (30-day climatic water balance, VPD, solar
289 radiation and wind speed) and climate (mean annual temperature (MAT), mean annual
290 precipitation (MAP) and mean daily solar radiation). In order to assess the independent and
291 interactive effects of all these variables on $\Delta T_{can-air}$ and to quantify their relative importance, we
292 followed the recommendations of Murray & Conner (2009). In brief, we first computed zeroth-
293 order correlations and eliminated those variables that presented near-zero correlations with
294 $\Delta T_{can-air}$. In a second step, we ran hierarchical partitioning of the variance for each family of
295 variables (forest structure, topographical, climatic and meteorological) to rank the importance of
296 these variables and discard those with small independent contributions (Mac Nally & Walsh,
297 2004). Selected variables were included in a *lmer* mixed model, for which we confirmed the
298 absence of multicollinearity effects using the *performance* R package (Lüdtke et al., 2020). Then,
299 we included in the final model those variables that improved the Akaike Information Criterion
300 (AIC) of the model (Akaike, 1974). Finally, we ran a general mixed model to assess the effects of
301 continuous environmental variables, in which we included functional group and stand composition
302 (pure versus mixed), hour of the observation, aspect of the plot and the MAP decile as random
303 factors. To compare the relative effects of model variables, we estimated *beta* (standardized)
304 coefficients. We also ran a similar model but with T_{can} as dependent variable, instead of
305 $\Delta T_{can-air}$.

306 The data on tree functional and hydraulic traits from Rosas et al. (2019) were obtained from
307 the same area and forest plot network as for the rest of data. However, trait data was only available
308 for the six most abundant species in the area, including two needleleaf Mediterranean trees
309 (NLMED; *Pinus halepensis* and *Pinus nigra*), one needleleaf montane tree (NLMON; *Pinus*
310 *sylvestris*), one broadleaf evergreen tree (*Quercus ilex*) and two broadleaf deciduous trees (*Fagus*
311 *sylvatica* and *Quercus pubescens*). Rosas et al. (2019) sampled 15 plots of each of these six species,
312 categorized across percentiles of the growing season climatic water balance (from dry to medium
313 to wet according to the <33rd, 33th–66th and >66th percentiles, respectively) calculated at the
314 species-specific level, for the whole forest plot network. This allowed us to estimate trait averages
315 across species and percentiles of climatic water balance (25 individuals in each combination of
316 species and type of climate). We categorized the climatic water balance of the growing season of

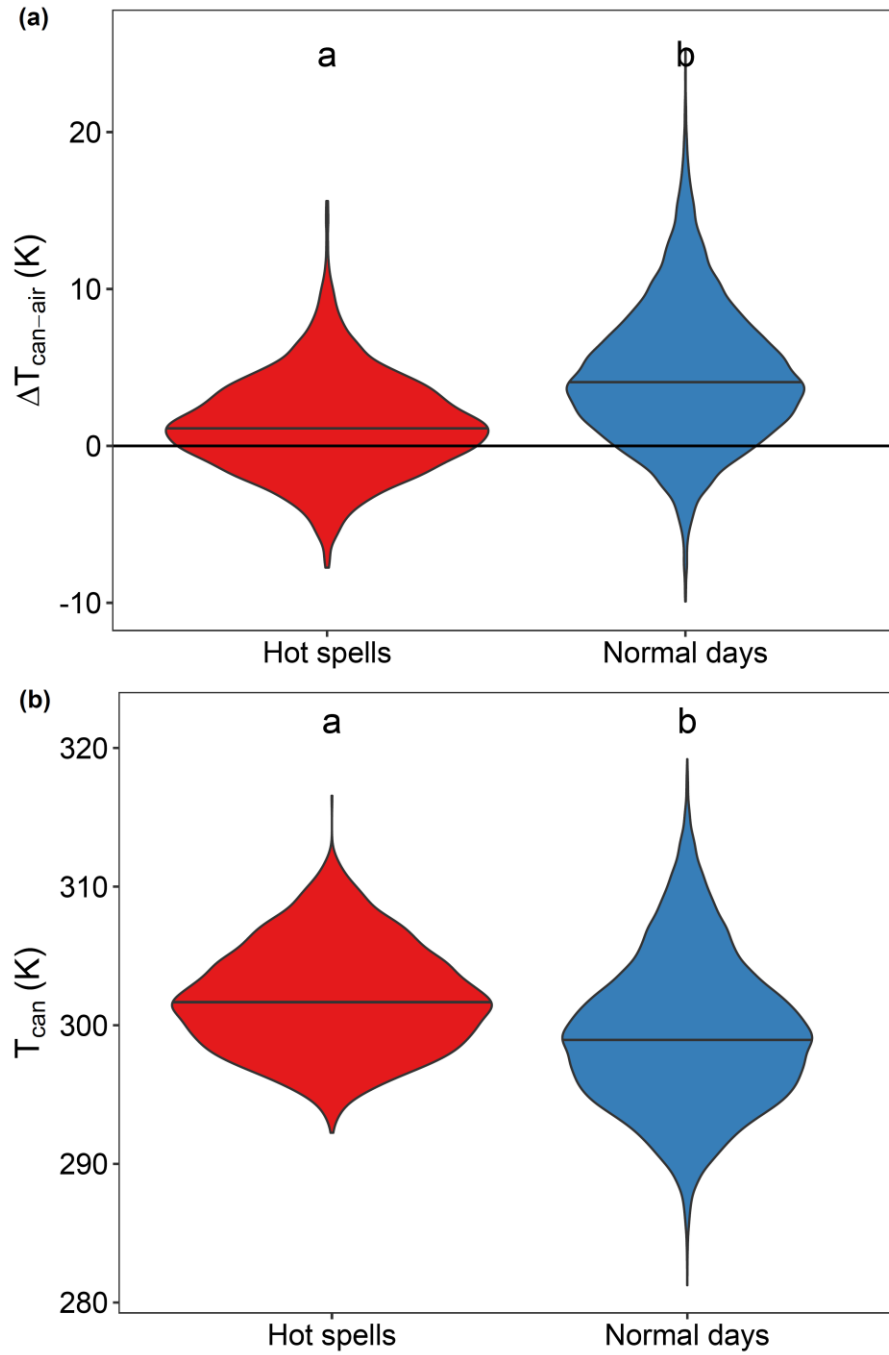
317 all plots classified as pure stands (>80% in basal area) of the six species studied in Rosas et al.
318 (2019), and computed group means (and their corresponding standard errors) of $\Delta T_{can-air}$
319 and T_{can} for all observations of the study period in normal days and hot spells, separately. We also
320 extracted the β coefficients of the correlation between $\Delta T_{can-air}$ and T_{can} and VPD, for the same
321 groups. We then calculated linear correlations of $\Delta T_{can-air}$, T_{can} , and their correlation with VPD
322 with the following traits: specific leaf area (SLA), xylem pressure at the 50% loss of conductivity
323 (P50), xylem pressure at the turgor loss point (ψ_{tlp}), stem specific conductivity (k_s), leaf specific
324 conductivity (k_l), leaf lifespan, leaf carbon isotopic composition ($\delta^{13}C$), wood density, leaf
325 thickness and Huber value (sapwood to leaf area ratio at the branch level). In a second step, we set
326 the “*species*” as random factor to determine whether inter-specific trait differences could explain
327 any potential correlation. All data processing and statistical analyses were carried out using the
328 software R, version 4.1.2. (R Core Team, 2021).

329

330 **3 Results**331 **3.1 Thermal Balance of Forests**

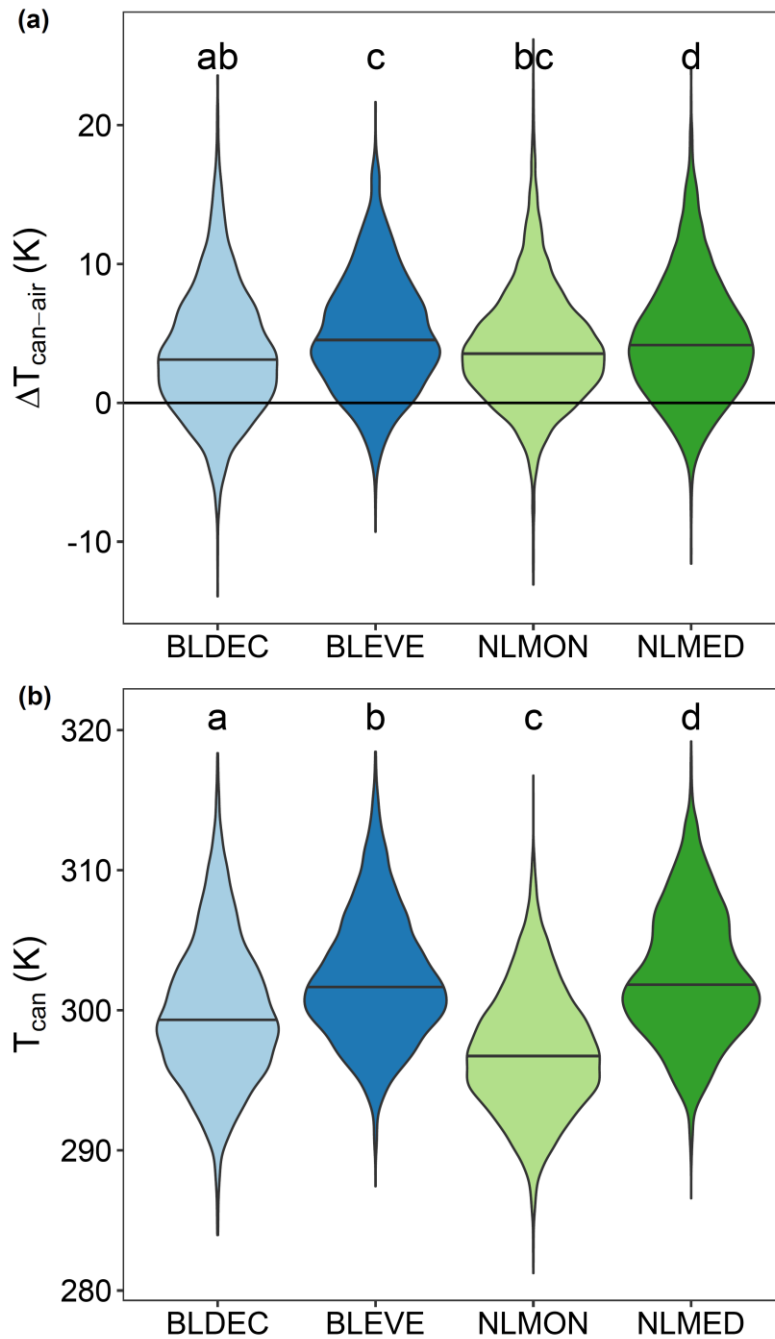
332 As estimated by the data collected by ECOSTRESS, T_{can} was on average (\pm se) 4.18 ± 0.03 K
333 warmer than T_{air} , ranging from -2.17 to 12.2 K (5th and 95th percentiles of $\Delta T_{can-air}$,
334 respectively), for June–September of 2018–2021 and from 9–15h UTC. There was a significant (p
335 < 0.001) effect of the hour of the measurement on T_{can} ; a peak in $\Delta T_{can-air}$ (8.12 ± 0.13 K) was
336 observed at 13h UTC coinciding with a peak in T_{can} (303.7 ± 0.15 K) (Fig. S1). In contrast, during
337 hot spells, the higher forest T_{can} , compared to normal days (301.9 ± 0.08 K vs 299.3 ± 0.03 K, p
338 < 0.001) was not accompanied by an also higher $\Delta T_{can-air}$, in fact $\Delta T_{can-air}$ was significantly
339 lower during hot spells (1.32 ± 0.07 K vs 4.50 ± 0.09 K, $p < 0.001$) (Fig. 2). Over the study period,
340 there were significant differences within the growing season among months in both $\Delta T_{can-air}$ and
341 T_{can} . First, observations for the month of July were very scarce (Fig. S2). For the rest of the
342 months, the warmest T_{can} was estimated for August, followed by June, and September (all
343 differences at least $p < 0.01$) (Fig. S3). For $\Delta T_{can-air}$, the largest values were estimated for the
344 months of September, followed by June, and August ($p < 0.01$) (Fig. S3). The species composition
345 of the stand also had significant influence on $\Delta T_{can-air}$. Mixed forests presented lower $\Delta T_{can-air}$
346 compared to pure forests (3.28 ± 0.05 K vs 4.53 ± 0.04 K, $p < 0.001$) (Fig. S4). Likewise, the
347 functional group of the dominant species also had a significant effect on the thermal balance of the
348 forest (Fig. 3). To test for differences in $\Delta T_{can-air}$, we accounted for the spatial and temporal
349 distribution of the observations using random factors and included the precipitation gradients as a
350 fixed factor. As a result, pairwise comparisons among the four different functional groups revealed
351 significant differences in $\Delta T_{can-air}$ ($p < 0.05$) that were not apparent in raw observations (Fig. 3a).
352 The statistical model revealed that NLMED had the lowest $\Delta T_{can-air}$. NLMON and BLDEC had
353 significantly higher $\Delta T_{can-air}$ than NLMED (Fig. 3a). BLEVE had the highest $\Delta T_{can-air}$, but not
354 significantly higher than NLMON. On the other hand, T_{can} was significantly different in each
355 group, being warmer in drier plots and following the thermal niche of each group (NLMED $>$
356 BLEVE $>$ BLDEC $>$ NLMON, Figure 3).

357



358

359 **Figure 2. The thermal balance ($\Delta T_{can-air}$) (a) and canopy temperature (T_{can}) (b) in hot spells**
360 **and normal days.** For both $\Delta T_{can-air}$ and T_{can} differences between hot spells and normal days
361 were significant, as noted by the different letters above each group of data points.



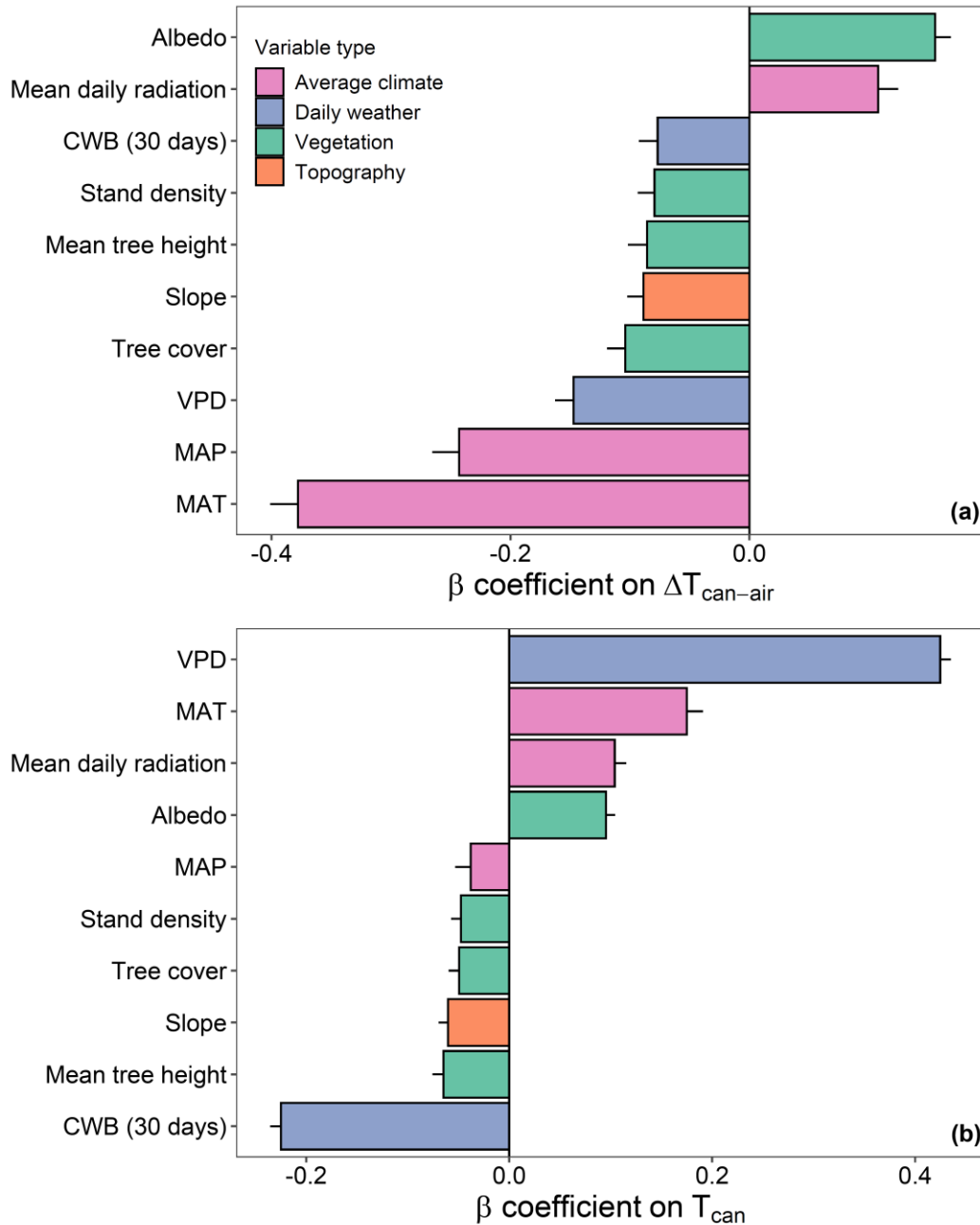
362

363 **Figure 3. The thermal balance ($\Delta T_{can-air}$) (a) and canopy temperature (T_{can}) (b) across**
 364 **different forest types.** Forest types are broadleaf deciduous (BLDEC), broadleaf evergreen
 365 (BLEVE), needleleaf montane (NLMON) and needleleaf Mediterranean (NLMED). Letters on top
 366 of each group of data points (a, b, c, or d) indicate significant differences between these groups as
 367 obtained with the GLMM. Note that statistical differences in $\Delta T_{can-air}$ estimated with GLMM do

368 not coincide with those derived by the medians of the observations of each group, because spatial
369 and temporal factors were included as random factors (see section 2.5 for details).

370 3.2 Drivers of the Spatiotemporal Variability in $\Delta T_{can-air}$ and T_{can}

371 We considered several plot-level structural, topographical, climatic, and daily meteorological
372 continuous predictors that could affect $\Delta T_{can-air}$ and T_{can} . By means of hierarchical partitioning
373 and generalized linear mixed models (see Sect. 2.5), we identified 11 variables that explained
374 15.4% of the variance of $\Delta T_{can-air}$ in the GLMM (40.5% including random effects). The
375 standardized β coefficients showed that the strongest correlation with $\Delta T_{can-air}$ was found for
376 MAT, followed by the effects of MAP, albedo, and VPD (Fig. 4a).



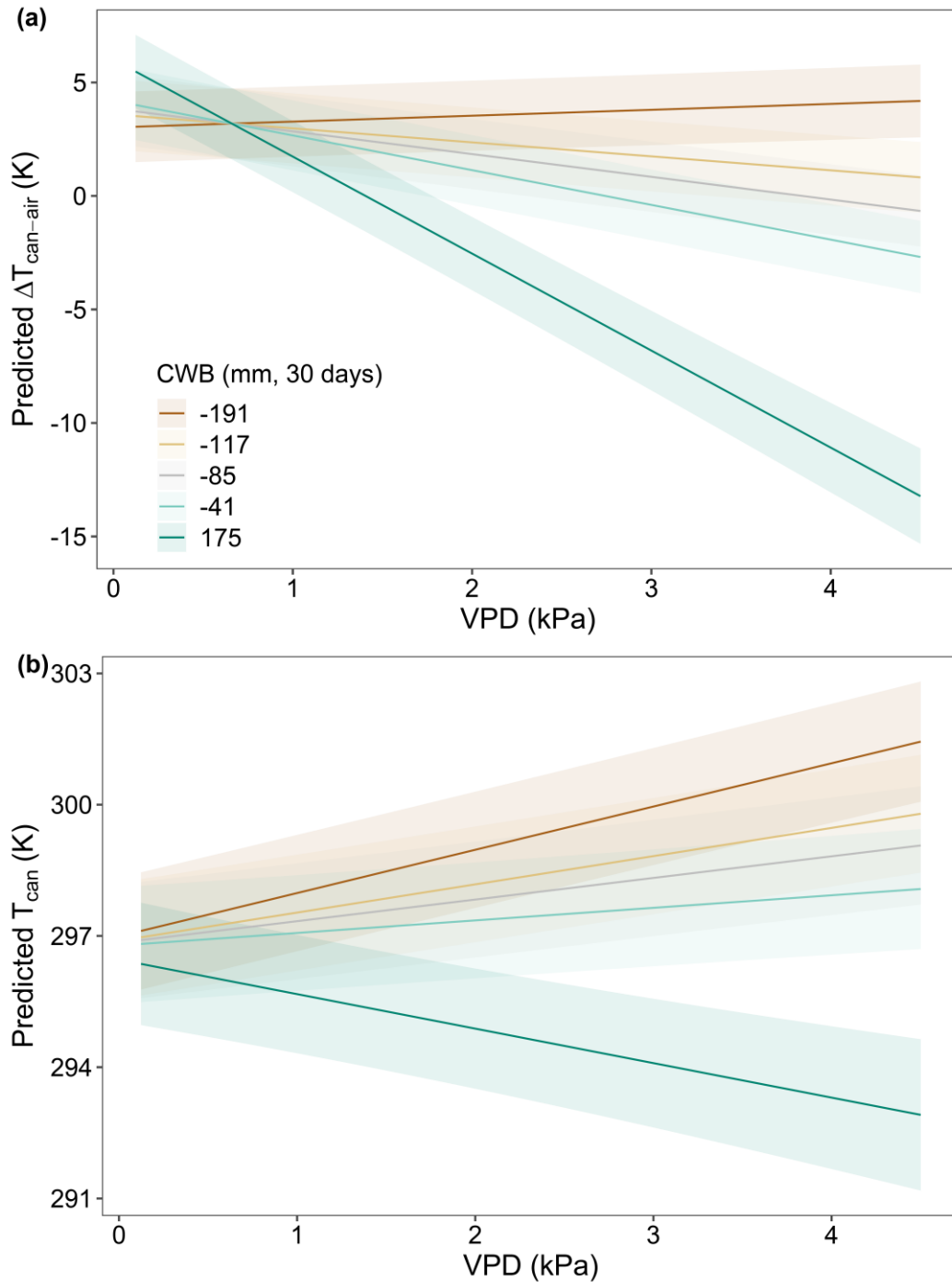
377

378 **Figure 4. Drivers of the thermal balance ($\Delta T_{can-air}$) and the canopy temperature (T_{can}).**
 379 Standardized β coefficients of the effect of the average climate (pink), daily weather (blue), forest
 380 structural (green) and topographical (orange) variables on $\Delta T_{can-air}$ (a) and T_{can} (b). Positive
 381 (negative) coefficients on $\Delta T_{can-air}$ imply correlations with warm (cool) T_{can} relative to T_{air} .
 382 Positive (negative) coefficients on T_{can} imply correlations with warmer (cooler) values of T_{can} .
 383 All variables included in the mixed model were significant ($p < 0.001$). Uncertainty bars are the

384 standard error of the mean, estimated for each individual effect. Effects are sorted based on their
385 beta coefficient.

386 According to the mixed model, $\Delta T_{can-air}$ tended to be closer to zero in tall forests (> 20 m) with
387 a high density and tree cover fraction, likely due to the higher surface roughness and aerodynamic
388 conductance (Fig. S5). Unsurprisingly, meteorological conditions were more strongly correlated
389 with $\Delta T_{can-air}$ than with T_{can} , due to the direct dependency of T_{air} on atmospheric
390 (thermo)dynamics. $\Delta T_{can-air}$ was closer to zero under high VPD, suggesting a control of warm
391 air advection over T_{air} . The climatic water balance (CWB) of the last 30 days was negatively
392 correlated with $\Delta T_{can-air}$, indicating that wetter conditions were associated with a $\Delta T_{can-air}$
393 closer to zero, as expected. The correlation with mean annual radiation was small, compared to
394 other climatic variables, but still, more radiation was associated with more positive $\Delta T_{can-air}$. In
395 addition, forests in steeper slopes had low $\Delta T_{can-air}$ compared to those in flatter areas. The
396 correlation of $\Delta T_{can-air}$ with VPD was significantly modified by the CWB (Fig. 5a). The negative
397 correlation of $\Delta T_{can-air}$ with VPD was stronger under wet conditions (positive CWB), whereas it
398 tended to vanish under drought due to the increase in T_{can} (Fig. 5).

399 The mixed model for T_{can} explained 71.2% of its variance, with fixed factors (the same that were
400 selected for $\Delta T_{can-air}$) explaining 64.2%. VPD was the factor with the highest correlation, even
401 more than other climatic variables. Although in this case the correlation with VPD was positive:
402 high VPD was associated with hotter T_{can} . We note that this may occur due to the partial stomatal
403 closure in response to high VPD, or due to the influence of heat advection constraining the ability
404 of the canopy to dissipate heat via sensible heat flux. On the other hand, CWB was associated with
405 cooler T_{can} . The interaction between VPD and CWB was significant for T_{can} . Model predictions
406 show that the positive correlation between VPD and T_{can} shifted to negative in wetter sites (Fig.
407 5b). In general, meteorological variables appeared to be more relevant than forest structural
408 variables for T_{can} (Fig. 4b). Still, we observed that cooler T_{can} was associated with tall forests with
409 high tree cover and stand density, whereas higher albedo was associated with hotter T_{can} .



410

411 **Figure 5. Interactive effects of VPD and climatic water balance (CWB) on the thermal**
 412 **balance ($\Delta T_{can-air}$) and the canopy temperature (T_{can}).** Model predictions of $\Delta T_{can-air}$ (a)
 413 and T_{can} (b) as a function of the vapor pressure deficit (VPD) and the climatic water balance
 414 (CWB) of the previous 30 days. Line colors illustrate different levels of CWB, from drier
 415 (negative) to wetter (positive) conditions. The shades around the lines correspond to the 95th

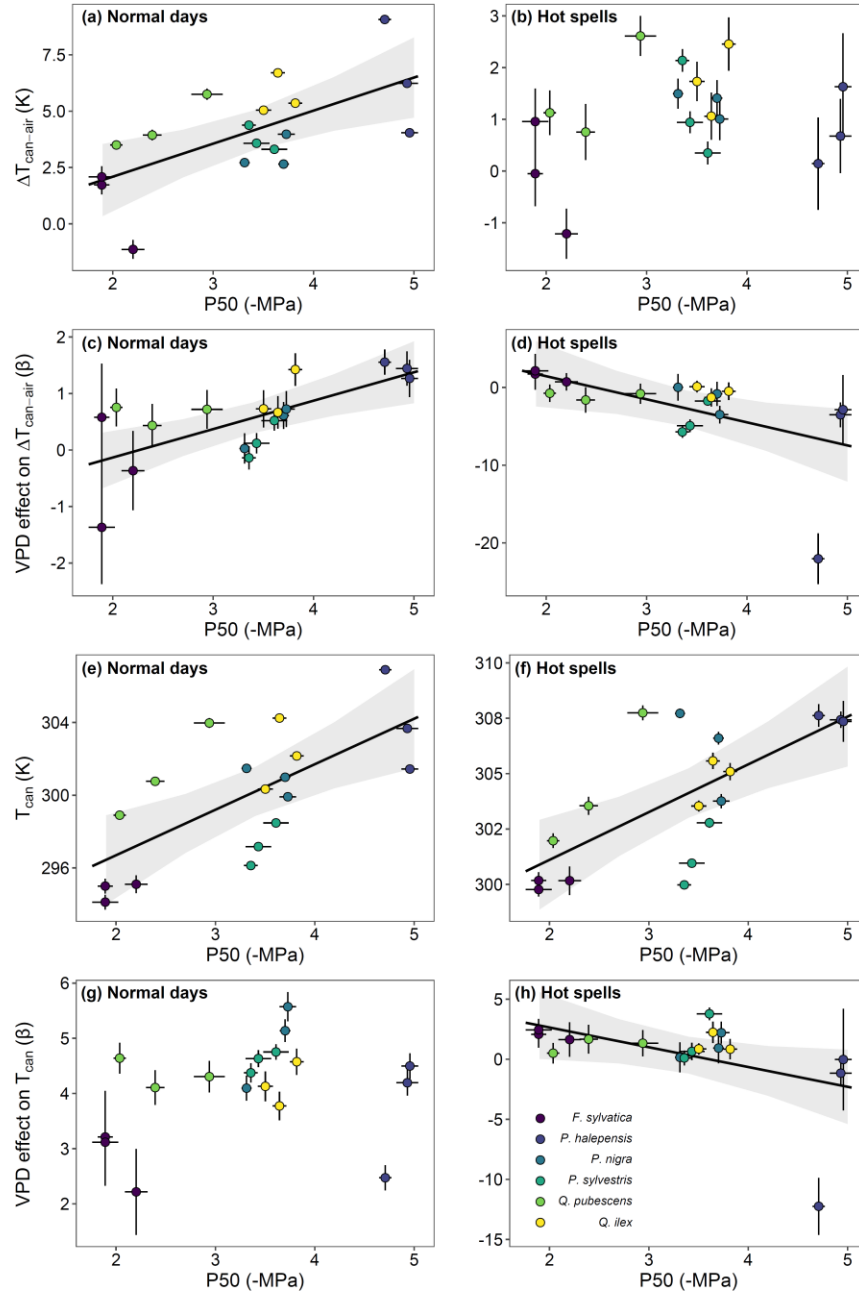
416 confidence intervals of the predicted $\Delta T_{can-air}$. The interaction between VPD and CWB was
 417 significant in the mixed models.

418 3.3 Effect of Plant Functional Traits on $\Delta T_{can-air}$ and T_{can}

419 Plant functional traits measured in Rosas et al. (2019) were associated with average
 420 $\Delta T_{can-air}$ across water availability gradients of the six most common tree species in the study
 421 area. We computed the correlation of plant functional traits with $\Delta T_{can-air}$ and found out that five
 422 out of the ten considered traits presented significant ($p < 0.05$) relationships in normal days (Table
 423 S3). After accounting for inter-specific variability (i.e., with the inclusion of *species* as a random
 424 factor in the models) the effect of plant functional traits on $\Delta T_{can-air}$ largely became not
 425 significant (Table S4). Still, $\Delta T_{can-air}$ showed a marginally significant relationship with the xylem
 426 pressure at 50% loss of conductivity (P50, Fig. 6a); trees with higher resistance to conductivity
 427 losses tended to have more positive values of $\Delta T_{can-air}$. We then tested if plant functional traits
 428 were associated with the response of $\Delta T_{can-air}$ to VPD. We found positive and significant effects
 429 of P50, leaf $\delta^{13}C$, specific leaf area (SLA), and the xylem pressure at turgor loss point (ψ_{tlp}) on the
 430 VPD- $\Delta T_{can-air}$ relationship. This means that forests dominated by species with higher water-use
 431 efficiency (higher $\delta^{13}C$), resistance to cavitation and turgor loss, and lower SLA also exhibited
 432 greater $\Delta T_{can-air}$ increases in response to high VPD, in normal days (Fig. 6c). Interestingly, the
 433 effect of P50 and leaf $\delta^{13}C$ on VPD- $\Delta T_{can-air}$ was significant but shifted their sign during hot
 434 spells (Fig. 6d, Table S3 and S4).

435 T_{can} was significantly associated with plant hydraulic traits of the most common species
 436 of the study area (see Table S5 for full results). During both normal periods and hot spells, T_{can}
 437 was warmer in forests dominated by species with higher resistance to conductivity losses (P50),
 438 more efficient water-use ($\delta^{13}C$) and more negative xylem pressure at the turgor loss point (ψ_{tlp})
 439 (Fig. 6e, f, Table S5). Thus, forests dominated by species with a vascular system that is more
 440 resistant to water stress tended to exhibit hotter T_{can} . The correlation of VPD with T_{can} was also
 441 dependent on leaf $\delta^{13}C$ during hot spells, but also on the leaf-to-sapwood area ratio (Huber value),
 442 leaf thickness, and leaf lifespan (Fig. 6h, Table S5). Forests dominated by species with higher
 443 resistance to conductivity losses (P50) were the only ones showing a decrease in T_{can} in response
 444 to the high VPD experienced during hot spells. In fact, those cases corresponded to the
 445 Mediterranean needleleaf *Pinus halepensis*.

446



447

448 **Figure 6. Correlation of the thermal balance of forests ($\Delta T_{can-air}$) and canopy temperature**
 449 **(T_{can}) with the xylem pressure at the 50% loss of conductivity (P50). Left panels (a, c, e and**
 450 **(a), the β coefficients of the vapor deficit pressure (VPD) effect on $\Delta T_{can-air}$ (b), T_{can} (c) and the**
 451 **β coefficients of the vapor deficit pressure (VPD) effect on T_{can} . Right panels (b, d, f and h) depict**
 452 **the same but for hot spells. Significant correlations are shown by solid lines and the corresponding**
 453 **p value is shown at the bottom right of each panel. Dashed lines represent marginally significant**
 454 **correlations. Fill colors show the different species included in the analysis.**
 455

456 **4 Discussion**457 4.1 Plot-scale Measurements of the Canopy Thermal Balance with ECOSTRESS
458

459 In this study, we leveraged the availability of high-resolution LST data from ECOSTRESS
460 to estimate the canopy thermal balance (as diagnosed by $\Delta T_{can-air}$) at a spatial scale that allows
461 integration with forest structural data from forest inventories and plant functional traits. On
462 average, our estimations of $\Delta T_{can-air}$ were slightly higher than those from montane coniferous
463 forests in both warm and cold seasons, but our range was similar (Javadian et al., 2022). This range
464 was broad, which could be caused by the wide ecoclimatic gradient covered by the study area,
465 including structurally and functionally different forests over a wide range of MAP (from 350 to
466 1300 mm, Table S1). Thus, our study included forests that are drier than those from studies in
467 other temperate areas where $\Delta T_{can-air}$ was estimated to be ca. 1 K lower (Still et al., 2022; Yi et
468 al., 2020). Importantly, the estimated $\Delta T_{can-air}$ derived from ECOSTRESS was comparable to
469 the $\Delta T_{can-air}$ obtained with *in-situ* thermal imaging for high elevation shrublands and meadows
470 (Blonder et al., 2020) and temperate needleleaf and broadleaf forests (Still et al., 2022). While the
471 area covered by infrared cameras is inevitably limited, their observations can be individual-
472 specific. On the contrary, analyses of the relationship between T_{air} and T_{can} from remote sensing
473 usually have a spatial resolution (ca. 0.5°) that exceeds the scale at which forest plot measurements
474 are collected. Our approach takes advantage of the best of these two approaches: the high spatial
475 coverage of satellite observations and the high spatial resolution provided by the novel
476 ECOSTRESS thermal sensor. This allows not only for a better understanding of how heat and
477 water exchange over time and space (Xiao et al., 2021), but also enables us to associate these
478 exchanges with fine-scale variations in forest structure and function (Cooley et al., 2022).

479 4.2 Heat Advection Influence on Forest $\Delta T_{can-air}$ Patterns
480

481 During hot spells, $\Delta T_{can-air}$ was significantly lower than in normal days, regardless of the
482 type of forest and its average climate (Fig. 2a). Hot spells in the Iberian Peninsula are usually
483 caused by the heat advection associated with Saharan air intrusions (Sousa et al., 2019). The warm
484 and dry air carried by these intrusions results in a lower $\Delta T_{can-air}$ driven by a sudden increase in
485 T_{air} . Hence, during hot spells although T_{can} was still higher than in normal days (Fig. 2b), the
486 increase experienced in T_{air} was even larger. As T_{air} increases, canopy-to-air sensible heat fluxes
487 will be inhibited (Still et al., 2021). As a result, the amplification of hot spells by local sensible
488 heat fluxes would be comparably unimportant, and thus the forest canopies would not have a
489 positive feedback on hot spell occurrence. Instead, the studied hot spells would be largely driven
490 by circulation and the advection of heat, rather than accompanied by changes in incoming radiation
491 and subsequent sensible heat fluxes (Fig. S6). Therefore, the response to hot spells of the forest
492 thermal balance in this Mediterranean region seems to contrast with the important influence of soil
493 desiccation found in higher latitudes (Schumacher et al., 2019; Teuling et al., 2010).

494 While heat advection appears to be a key component of the forest thermal balance, we still
495 found that $\Delta T_{can-air}$ was a function of local climatic gradients and daily meteorological conditions
496 across the studied forest plot network. Spatial variability in rainfall and solar radiation exerted
497 negative and positive effects, respectively, on both $\Delta T_{can-air}$ and T_{can} . This can be expected
498 because solar radiation warms the surface (T_{can}), and the availability of water governs the
499

500 partitioning of that radiation between sensible and latent heat fluxes. T_{can} was on average warmer
 501 in locations with warmer mean annual temperatures (Fig. 4b). During hot spells, heat advection
 502 results in decreases in $\Delta T_{can-air}$. This explains the negative correlation between VPD and MAT
 503 with $\Delta T_{can-air}$ (Fig. 4a). High VPD during hot spells coincides in space and time with low
 504 $\Delta T_{can-air}$, as opposed to what could be expected if the high VPD was a response to dry and warm
 505 surfaces. In summary, increases in T_{air} are externally driven by advection, and not by local
 506 sensible heat fluxes because in that case, we should have observed a positive relationship between
 507 $\Delta T_{can-air}$ and VPD.

508
 509 VPD is one of the main drivers of canopy transpiration (Flo et al., 2021; Grossiord et al.,
 510 2020), but transpiration responds to high VPD range from strong decreases to strong increases as
 511 a function of the plants' water use strategy (Massmann et al., 2019). Initially, in moist temperate
 512 forests, moderate increases in VPD may enhance transpiration rates and cool down the canopy (Yi
 513 et al., 2020). Yet, in water-limited areas, such as the one studied here, canopy transpiration tends
 514 to decline with increases in VPD (Duursma et al., 2014; Flo et al., 2021). This agrees with the
 515 positive correlation between high VPD and warm T_{can} that we observed under dry conditions (Fig.
 516 5b) showing that high VPD prevents the transpiration-driven cooling of the canopy. Yet, increasing
 517 VPD should still result in cooler canopies when water is still available for plants (Fig. 5b). Indeed,
 518 we found lower $\Delta T_{can-air}$ and cooler T_{can} under wetter conditions (Fig. 4), which we attributed
 519 to the increase in transpiration when the soil is moist in these water-limited environments. Our
 520 results are consistent with observations from tropical regions, where water availability in the upper
 521 soil layers strongly controls surface temperature (Green et al., 2022). Similarly, in temperate
 522 regions, the deeper root systems of forests compared to grasslands also result in more
 523 transpirational cooling and lower temperatures (Lansu et al., 2020; Teuling et al., 2010; Zhang et
 524 al., 2020), emphasizing the importance of root water uptake for predicting vegetation-atmosphere
 525 feedbacks (Barbeta & Peñuelas, 2017; Cabon et al., 2018). Access to deep soil water allows the
 526 vegetation to dissipate heat through evaporation from the leaves, thus avoiding overheating,
 527 decreasing T_{can} and sensible heat fluxes (Krich et al., 2022). Under wet soils and high VPD, our
 528 model predicted that $\Delta T_{can-air}$ would become negative, i.e., T_{can} could be cooler than T_{air} (Fig.
 529 5a). Yet, previous studies have shown that a negative $\Delta T_{can-air}$ in clear sky days is rare for
 530 temperate forests and that it can only be expected in systems such as rice paddies where water
 531 supply is unlimited (Still et al., 2022), or during rain events (van Dijk et al., 2015). Because our
 532 remotely sensed T_{air} is only available for clear sky days, the predicted low $\Delta T_{can-air}$ was most
 533 likely caused by the occurrence of heat advection in combination with sufficient soil water
 534 availability to supply transpiration during hot spells, instead of by a VPD-induced transpiration
 535 increase, as indicated above.

536 4.3 Biotic controls on forest $\Delta T_{can-air}$

537 We found significant but quantitatively small differences in $\Delta T_{can-air}$ among forests
 538 dominated by species belonging to different functional groups (Fig. 3a). For example, the thermal
 539 balance of needleleaf montane forests did not differ from that of broadleaf deciduous, despite their
 540 slightly different climatic niches (Table S1). $\Delta T_{can-air}$ differed among forests dominated by
 541 functional groups occupying contrasting climatic niches (see summer PPET in Table S1), but also
 542 presenting substantial structural differences (Table S2). For example, we found that $\Delta T_{can-air}$ was
 543 higher in broadleaf evergreen forests than in the also drought-adapted needleleaf Mediterranean

544 (Table S1, Fig. 3b). Still, $\Delta T_{can-air}$ in broadleaf evergreen forests was not statistically different to
 545 the structurally and climatically different needleleaf montane forests. The differences in T_{can}
 546 between functional groups are constrained by the background climatic conditions (i.e., gradients
 547 in MAT), but for $\Delta T_{can-air}$ the differences among groups were possibly modified by contrasting
 548 surface properties and forest functioning. This was further confirmed by the analysis of the drivers
 549 of $\Delta T_{can-air}$ showing significant effects of MAP and MAT, but also of forest structural variables
 550 such as albedo, mean tree height or tree cover (Fig. 4). The discrete nature of functional groups
 551 may be too limiting to describe continuous fluxes such as those involved in the forest thermal
 552 balance (Bodegom et al., 2012). Indeed, the intra-group variability in $\Delta T_{can-air}$ was high within
 553 all groups (Fig. 3), in agreement with previous studies suggesting that site-specific conditions may
 554 be more relevant than plant functional groups (Wang et al., 2019) or leaf-level traits (Blonder et
 555 al., 2020) for the surface energy balance.

556 The structure of forests appeared almost as determinant as daily meteorological conditions
 557 for $\Delta T_{can-air}$. In contrast, T_{can} mostly varied as a function of daily VPD and CWB (Fig. 4). As
 558 hypothesized, we found significant correlations of forest structural variables that determine heat
 559 dissipation mechanisms. The model showed that tall and dense forests with a canopy fully covering
 560 the ground maintained a cooler T_{can} relative to T_{air} , compared to forests with short trees with
 561 sparse stems and canopies. Albedo affected positively both $\Delta T_{can-air}$ and T_{can} . This positive effect
 562 on $\Delta T_{can-air}$ or T_{can} may be the consequence of the higher albedos of forests adapted to warmer
 563 temperatures and with a more conservative water use (Muller et al., 2021). Albedo is indeed lower
 564 in montane needleleaf forests, compared to Mediterranean needleleaf ones (Table S2). Similarly,
 565 $\Delta T_{can-air}$ is higher in those stands occupying drier areas and composed by species with functional
 566 traits associated with a more efficient water use and a higher resistance to drought (Table S3 and
 567 Fig. 6a), as expected. In addition, the response of $\Delta T_{can-air}$ to VPD is clearly positive in drier
 568 stands (Fig. 6c). Interestingly, this relationship was reversed during hot spells (Table S3 and Fig.
 569 6d). During hot spells, the $\Delta T_{can-air}$ did not respond to VPD in drought-sensitive species such as
 570 *F. sylvatica* (Fig. 6d). In contrast, $\Delta T_{can-air}$ and T_{can} were disproportionately reduced by VPD
 571 during hot spells in drought-resistant conifer species, such as *P. halepensis* (Sánchez-Costa et al.,
 572 2015). This trait-mediated disparity in species-specific (and intra-specific) response to VPD during
 573 hot spells is in agreement with the observations of high transpiration during extremely high VPD
 574 conditions in Australian Mediterranean woodlands (Krich et al., 2022), but only for certain
 575 ecosystems with access to groundwater. The capacity to tap on deep water sources in
 576 Mediterranean ecosystem may be key to sustain transpiration under high VPD and heat stress.

577 **5. Conclusions**

578 Here we used a novel approach combining high-resolution remotely-sensed land surface
 579 temperature with a suite of ground-based structural and functional forest data to investigate the
 580 environmental determinants of the forest thermal balance for a Mediterranean region. We found
 581 that the forest thermal balance during hot spells was more dependent on heat advection episodes
 582 suddenly increasing T_{air} than on T_{can} . This pattern is fundamentally different to the strong
 583 influence of surface responses in less water-limited regions (Lansu et al., 2020; Teuling et al.,
 584 2010; Wang et al., 2019). In fact, background climatic conditions explained a significant part of
 585 the variability in $\Delta T_{can-air}$ in our study area, which also contains relatively moist forests
 586 analogous to those in temperate regions, as central Europe. Furthermore, we found that climatic
 587 water availability and the plant water use strategy exert additional controls on the forest thermal

588 balance, probably through transpiration cooling. The coordination of rooting depth and other plant
589 functional traits linked to water-use strategies (Illuminati et al., 2022) may underlie the association
590 of the considered traits with the response to increased VPD during hot spells, that included canopy
591 cooling in the driest stands of the most drought-resistant species (Fig. 6h). Finally, we also showed
592 that forest structural characteristics related to surface roughness such as tree height and cover,
593 stand density, and albedo also influence the forest thermal balance, as they affect heat dissipation
594 mechanisms (Muller et al., 2021). Therefore, our results demonstrate that the integration of
595 functional traits and forest structure over relevant spatial scales could improve our ability to
596 understand and model land–atmosphere feedbacks in forested regions.

597 **Acknowledgments**

598 AB acknowledges a Beatriu de Pinós MSCA-COFUND postdoctoral grant from the Government
599 of Catalonia (2019BP00193). AB and JC received funding from the Spanish Ministry of Science
600 (Grant MICROCLIM, PID2020-117636GB-C21). D.G.M. is supported by the European Research
601 Council (ERC), grant agreement 101088405 (HEAT). TEG received funding from the Spanish
602 Ministry of Science (Grant PHLISCO, PID2019-107817RB-I00). We would like to thank Teresa
603 Rosas, Jordi Martínez-Vilalta and Maurizio Mencuccini by providing the data on plant hydraulic
604 traits and Víctor Granda for his help with the data from the Catalan Forest Laboratory. The authors
605 declare that they do not have any competing interest.

606

607 **Open Research**

608 The data that support the findings of this study are openly available in the Zenodo repository at
609 <https://zenodo.org/record/7254572>, full details are given in the next section (Barbeta et al., 2022).

610

611 **References**

- 612
613 Akaike, H. (1974). A New Look at the Statistical Model Identification. *IEEE Transactions on Automatic Control*,
614 *19*(6), 716–723. <https://doi.org/10.1109/TAC.1974.1100705>
- 615 Anderegg, W. R. L., Konings, A. G., Trugman, A. T., Yu, K., Bowling, D. R., Gabbitas, R., et al. (2018). Hydraulic
616 diversity of forests regulates ecosystem resilience during drought. *Nature*, *561*(7724), 538–541.
617 <https://doi.org/10.1038/s41586-018-0539-7>
- 618 Anderegg, W. R. L., Trugman, A. T., Bowling, D. R., Salvucci, G., & Tuttle, S. E. (2019). Plant functional traits and
619 climate influence drought intensification and land–atmosphere feedbacks. *Proceedings of the National*
620 *Academy of Sciences of the United States of America*, *116*(28), 14071–14076.
621 <https://doi.org/10.1073/pnas.1904747116>

- 622 Bagley, J. E., Kueppers, L. M., Billesbach, D. P., Williams, I. N., Biraud, S. C., & Torn, M. S. (2017). The influence
623 of land cover on surface energy partitioning and evaporative fraction regimes in the U.S. Southern Great
624 Plains. *Journal of Geophysical Research*, 122(11), 5793–5807. <https://doi.org/10.1002/2017JD026740>
- 625 Barbeta, A., & Peñuelas, J. (2017). Relative contribution of groundwater to plant transpiration estimated with stable
626 isotopes. *Scientific Reports*, 7(1), 1–10. <https://doi.org/10.1038/s41598-017-09643-x>
- 627 Barbeta, A., Miralles, D. G., Mendiola, L., Gimeno, T. E., Sabaté, S., & Carnicer, J. (2022). Thermal balance of
628 forests in the Mediterranean-temperate ecotone. <https://doi.org/10.5281/ZENODO.7254572>
- 629 Bates, D., Mächler, M., Bolker, B. M., & Walker, S. C. (2015). Fitting linear mixed-effects models using lme4.
630 *Journal of Statistical Software*, 67(1), 1–48. <https://doi.org/10.18637/jss.v067.i01>
- 631 Beck, H. E., Zimmermann, N. E., McVicar, T. R., Vergopolan, N., Berg, A., & Wood, E. F. (2018). Present and
632 future köppen-geiger climate classification maps at 1-km resolution. *Scientific Data*, 5, 1–12.
633 <https://doi.org/10.1038/sdata.2018.214>
- 634 Blonder, B., Escobar, S., Kapás, R. E., & Michaletz, S. T. (2020). Low predictability of energy balance traits and
635 leaf temperature metrics in desert, montane and alpine plant communities. *Functional Ecology*, 34(9),
636 1882–1897. <https://doi.org/10.1111/1365-2435.13643>
- 637 Bodegom, P. M. Van, Douma, J. C., Witte, J. P. M., Ordoñez, J. C., Bartholomeus, R. P., Aerts, R., et al. (2012).
638 Going beyond limitations of plant functional types when predicting global ecosystem – atmosphere fluxes :
639 exploring the merits of traits-based approaches, 625–636. [https://doi.org/10.1111/j.1466-](https://doi.org/10.1111/j.1466-8238.2011.00717.x)
640 [8238.2011.00717.x](https://doi.org/10.1111/j.1466-8238.2011.00717.x)
- 641 Bonan, G. (2015). *Ecological Climatology: Concepts and Applications* (3rd ed.). Cambridge: Cambridge University
642 Press. <https://doi.org/10.1017/CBO9781107339200>
- 643 Cabon, A., Martínez-Vilalta, J., Martínez de Aragón, J., Poyatos, R., & De Cáceres, M. (2018). Applying the eco-
644 hydrological equilibrium hypothesis to model root distribution in water-limited forests. *Ecohydrology*,
645 11(7), e2015. <https://doi.org/10.1002/eco.2015>
- 646 De Cáceres, M., Martin-StPaul, N., Turco, M., Cabon, A., & Granda, V. (2018). Estimating daily meteorological
647 data and downscaling climate models over landscapes. *Environmental Modelling and Software*,
648 108(August), 186–196. <https://doi.org/10.1016/j.envsoft.2018.08.003>

- 649 Canadell, J. G., Monteiro, P. M. S., Costa, M. H., da Cunha, L., Cox, P. M., Eliseev, A. V., et al. (2021). Global
650 Carbon and other Biogeochemical Cycles and Feedbacks. In V. Masson-Delmotte, P. Zhai, A. Pirani, S. L.
651 Connors, C. Péan, S. Berger, et al. (Eds.), *Climate Change 2021: The Physical Science Basis. Contribution*
652 *of Working Group I to the Sixth Assessment Report of the Intergovernmental Panel on Climate Change* (pp.
653 673–816). Cambridge, United Kingdom and New York, NY, USA: Cambridge University Press.
654 <https://doi.org/10.1017/9781009157896.007>
- 655 Cescatti, A., Marcolla, B., Santhana Vannan, S. K., Pan, J. Y., Román, M. O., Yang, X., et al. (2012).
656 Intercomparison of MODIS albedo retrievals and in situ measurements across the global FLUXNET
657 network. *Remote Sensing of Environment*, 121, 323–334. <https://doi.org/10.1016/j.rse.2012.02.019>
- 658 Cooley, S. S., Fisher, J. B., & Goldsmith, G. R. (2022). Convergence in water use efficiency within plant functional
659 types across contrasting climates. *Nature Plants*, 8(April). <https://doi.org/10.1038/s41477-022-01131-z>
- 660 van Dijk, A. I. J. M., Gash, J. H., van Gorsel, E., Blanken, P. D., Cescatti, A., Emmel, C., et al. (2015). Rainfall
661 interception and the coupled surface water and energy balance. *Agricultural and Forest Meteorology*, 214–
662 215, 402–415. <https://doi.org/10.1016/j.agrformet.2015.09.006>
- 663 Drumond, A., Marengo, J., Ambrizzi, T., Nieto, R., Moreira, L., & Gimeno, L. (2014). The role of the Amazon
664 Basin moisture in the atmospheric branch of the hydrological cycle: A Lagrangian analysis. *Hydrology and*
665 *Earth System Sciences*, 18(7), 2577–2598. <https://doi.org/10.5194/hess-18-2577-2014>
- 666 Duursma, R. A., Barton, C. V. M., Lin, Y.-S., Medlyn, B. E., Eamus, D., Tissue, D. T., et al. (2014). The peaked
667 response of transpiration rate to vapour pressure deficit in field conditions can be explained by the
668 temperature optimum of photosynthesis. *Agricultural and Forest Meteorology*, 189–190, 2–10.
669 <https://doi.org/10.1016/j.agrformet.2013.12.007>
- 670 Ellison, D., Morris, C. E., Locatelli, B., Sheil, D., Cohen, J., Murdiyarsa, D., et al. (2017). Trees, forests and water:
671 Cool insights for a hot world. *Global Environmental Change*, 43, 51–61.
- 672 Fauset, S., Freitas, H. C., Galbraith, D. R., Sullivan, M. J. P., Aidar, M. P. M., Joly, C. A., et al. (2018). Differences
673 in leaf thermoregulation and water use strategies between three co-occurring Atlantic forest tree species.
674 *Plant Cell and Environment*, 41(7), 1618–1631. <https://doi.org/10.1111/pce.13208>

- 675 Fischer, E. M., Seneviratne, S. I., Lüthi, D., & Schär, C. (2007). Contribution of land-atmosphere coupling to recent
676 European summer heat waves. *Geophysical Research Letters*, *34*(6), 1–6.
677 <https://doi.org/10.1029/2006GL029068>
- 678 Fisher, J. B., Lee, B., Purdy, A. J., Halverson, G. H., Dohlen, M. B., Cawse-Nicholson, K., et al. (2020).
679 ECOSTRESS: NASA's Next Generation Mission to Measure Evapotranspiration From the International
680 Space Station. *Water Resources Research*, *56*(4), 1–20. <https://doi.org/10.1029/2019WR026058>
- 681 Flo, V., Martinez-Vilalta, J., Granda, V., Mencuccini, M., & Poyatos, R. (2021). Vapour pressure deficit is the main
682 driver of tree canopy conductance across biomes. *Agricultural and Forest Meteorology*, *322*, 109029.
683 <https://doi.org/10.1002/essoar.10508049.1> |
- 684 Forzieri, G., Alkama, R., Miralles, D. G., & Cescatti, A. (2017). Satellites reveal contrasting responses of regional
685 climate to the widespread greening of Earth, *1184*(June), 1180–1184.
- 686 Forzieri, G., Miralles, D. G., Ciais, P., Alkama, R., Ryu, Y., Duveiller, G., et al. (2020). Increased control of
687 vegetation on global terrestrial energy fluxes. *Nature Climate Change*, *10*(4), 356–362.
688 <https://doi.org/10.1038/s41558-020-0717-0>
- 689 Gerken, T., Ruddell, B. L., Yu, R., Stoy, P. C., & Drewry, D. T. (2019). Robust observations of land-to-atmosphere
690 feedbacks using the information flows of FLUXNET. *Npj Climate and Atmospheric Science*, *2*(1).
691 <https://doi.org/10.1038/s41612-019-0094-4>
- 692 Grace, J. (1988). Plant Response to Wind. In *Agriculture, Ecosystems and Environment* (Vol. 22/23, pp. 71–88).
693 Amsterdam, Netherlands: Elsevier Science Publishers B.V.
- 694 Green, J. K., Ballantyne, A., Abramoff, R., Gentine, P., Makowski, D., & Ciais, P. (2022). Surface temperatures
695 reveal the patterns of vegetation water stress and their environmental drivers across the tropical Americas.
696 *Global Change Biology*, *28*(9), 2940–2955. <https://doi.org/10.1111/gcb.16139>
- 697 Grossiord, C., Buckley, T. N., Cernusak, L. A., Novick, K. A., Poulter, B., Siegwolf, R. T. W., et al. (2020). Plant
698 responses to rising vapor pressure deficit. *New Phytologist*, *226*(6), 1550–1566.
699 <https://doi.org/10.1111/nph.16485>
- 700 Hulley, G. C., Göttsche, F. M., Rivera, G., Hook, S. J., Freepartner, R. J., Martin, M. A., et al. (2022). Validation
701 and Quality Assessment of the ECOSTRESS Level-2 Land Surface Temperature and Emissivity Product.

- 702 *IEEE Transactions on Geoscience and Remote Sensing*, 60, 1–23.
703 <https://doi.org/10.1109/TGRS.2021.3079879>
- 704 Illuminati, A., Querejeta, J. I., Pías, B., Escudero, A., & Matesanz, S. (2022). Coordination between water uptake
705 depth and the leaf economic spectrum in a Mediterranean shrubland. *Journal of Ecology*, (January), 1–13.
706 <https://doi.org/10.1111/1365-2745.13909>
- 707 IPCC. (2021). *Climate Change 2021: The Physical Science Basis. Contribution of Working Group I to the Sixth*
708 *Assessment Report of the Intergovernmental Panel on Climate Change*. Cambridge, United Kingdom and
709 New York, NY, USA: Cambridge University Press. <https://doi.org/10.1017/9781009157896>
- 710 Javadian, M., Smith, W. K., Lee, K., Knowles, J. F., Scott, R. L., Fisher, J. B., et al. (2022). Canopy Temperature Is
711 Regulated by Ecosystem Structural Traits and Captures the Ecohydrologic Dynamics of a Semiarid Mixed
712 Conifer Forest Site. *Journal of Geophysical Research: Biogeosciences*, 127(2), 1–15.
713 <https://doi.org/10.1029/2021JG006617>
- 714 Keune, J., & Miralles, D. G. (2019). A Precipitation Recycling Network to Assess Freshwater Vulnerability:
715 Challenging the Watershed Convention. *Water Resources Research*, 55(11), 9947–9961.
- 716 Knauer, J., El-Madany, T. S., Zaehle, S., & Migliavacca, M. (2018). Bigleaf—An R package for the calculation of
717 physical and physiological ecosystem properties from eddy covariance data. *PLoS ONE*, 13(8), 1–26.
718 <https://doi.org/10.1371/journal.pone.0201114>
- 719 Krich, C., Mahecha, M. D., Migliavacca, M., De Kauwe, M. G., Griebel, A., Runge, J., & Miralles, D. G. (2022).
720 Decoupling between ecosystem photosynthesis and transpiration: A last resort against overheating.
721 *Environmental Research Letters*, 17(4), 44013. <https://doi.org/10.1088/1748-9326/ac583e>
- 722 Lansu, E. M., van Heerwaarden, C. C., Stegehuis, A. I., & Teuling, A. J. (2020). Atmospheric Aridity and Apparent
723 Soil Moisture Drought in European Forest During Heat Waves. *Geophysical Research Letters*, 47(6).
724 <https://doi.org/10.1029/2020GL087091>
- 725 Lenth, R., Singmann, H., Love, J., Buerkner, P., & Herve, M. (2018). Emmeans: Estimated marginal means, aka
726 least-squares means. *R Package Version*, 1(1), 3.
- 727 Llebot, J. E. (2005). *Informe sobre el canvi climàtic a Catalunya*. Barcelona.
- 728 Lüdecke, D., Makowski, D., Waggoner, P., & Patil, I. (2020). Package “performance”: Assessment of Regression
729 Models Performance. *CRAN.R*.

- 730 Martín Vide, J. (coord.). (2016). Tercer Informe sobre el canvi climàtic de Catalunya. Insitut d'Estudis Catalans i
731 Generalitat de Catalunya.
- 732 Massmann, A., Gentine, P., & Lin, C. (2019). When Does Vapor Pressure Deficit Drive or Reduce
733 Evapotranspiration? *Journal of Advances in Modeling Earth Systems*, *11*(10), 3305–3320.
734 <https://doi.org/10.1029/2019MS001790>
- 735 Meier, R., Davin, E. L., Swenson, S. C., Lawrence, D. M., & Schwaab, J. (2019). Biomass heat storage dampens
736 diurnal temperature variations in forests. *Environmental Research Letters*, *14*(8), 084026.
737 <https://doi.org/10.1088/1748-9326/ab2b4e>
- 738 Migliavacca, M., Musavi, T., Mahecha, M. D., Nelson, J. A., Knauer, J., Baldocchi, D. D., et al. (2021). The three
739 major axes of terrestrial ecosystem function. *Nature*, *598*(7881), 468–472. [https://doi.org/10.1038/s41586-](https://doi.org/10.1038/s41586-021-03939-9)
740 [021-03939-9](https://doi.org/10.1038/s41586-021-03939-9)
- 741 Miralles, D. G., Teuling, A. J., Van Heerwaarden, C. C., & De Arellano, J. V. G. (2014). Mega-heatwave
742 temperatures due to combined soil desiccation and atmospheric heat accumulation. *Nature Geoscience*,
743 *7*(5), 345–349. <https://doi.org/10.1038/ngeo2141>
- 744 Miralles, D. G., Gentine, P., Seneviratne, S. I., & Teuling, A. J. (2019). Land–atmospheric feedbacks during
745 droughts and heatwaves: state of the science and current challenges. *Annals of the New York Academy of*
746 *Sciences*, *1436*(1), 19–35. <https://doi.org/10.1111/nyas.13912>
- 747 Moyano, M. C., Garcia, M., Palacios-Orueta, A., Tornos, L., Fisher, J. B., Fernández, N., et al. (2018). Vegetation
748 Water Use Based on a Thermal and Optical Remote Sensing Model in the Mediterranean Region of
749 Doñana. *Remote Sensing*, *10*(7), 1105. <https://doi.org/10.3390/rs10071105>
- 750 Muller, J. D., Rotenberg, E., Tatarinov, F., Oz, I., & Yakir, D. (2021). Evidence for efficient nonevaporative leaf-to-
751 air heat dissipation in a pine forest under drought conditions. *New Phytologist*, *232*(6), 2254–2266.
752 <https://doi.org/10.1111/nph.17742>
- 753 Murray, K., & Conner, M. M. (2009). Methods to quantify variable importance: implications for the analysis of
754 noisy ecological data. *Ecology*, *90*(2), 348–355. <https://doi.org/10.1890/0012-9658-90.5.1425>
- 755 Mac Nally, R., & Walsh, C. J. (2004). Hierarchical partitioning public-domain software. *Biodiversity and*
756 *Conservation*, *13*(3), 659–660. <https://doi.org/10.1023/B:BIOC.0000009515.11717.0b>

- 757 Nemani, R. R., Running, S. W., Pielke, R. A., & Chase, T. N. (1996). Global vegetation cover changes from coarse
758 resolution satellite data. *Journal of Geophysical Research Atmospheres*, *101*(D3), 7157–7162.
759 <https://doi.org/10.1029/95JD02138>
- 760 O'Connor, J. C., Dekker, S. C., Staal, A., Tuinenburg, O. A., Rebel, K. T., & Santos, M. J. (2021). Forests buffer
761 against variations in precipitation. *Global Change Biology*, *27*(19), 4686–4696.
762 <https://doi.org/10.1111/gcb.15763>
- 763 de Oliveira, G., Brunsell, N. A., Moraes, E. C., Shimabukuro, Y. E., dos Santos, T. V., von Randow, C., et al.
764 (2019). Effects of land-cover changes on the partitioning of surface energy and water fluxes in Amazonia
765 using high-resolution satellite imagery. *Ecohydrology*, *12*(6), 1–18. <https://doi.org/10.1002/eco.2126>
- 766 Pitman, A. J. (2003). The evolution of, and revolution in, land surface schemes designed for climate models.
767 *International Journal of Climatology*, *23*(5), 479–510. <https://doi.org/10.1002/joc.893>
- 768 R Core Team. (2021). R: A Language and Environment for Statistical Computing. Vienna, Austria: R Foundation
769 for Statistical Computing.
- 770 Roces-díaz, J. V., Vayreda, J., Banqué-casanovas, M., Cusó, M., Anton, M., Bonet, J. A., et al. (2018). Assessing the
771 distribution of forest ecosystem services in a highly populated Mediterranean region. *Ecological Indicators*,
772 *93*(October 2016), 986–997. <https://doi.org/10.1016/j.ecolind.2018.05.076>
- 773 Rosas, T., Mencuccini, M., Barba, J., Cochard, H., Saura-Mas, S., & Martínez-Vilalta, J. (2019). Adjustments and
774 coordination of hydraulic, leaf and stem traits along a water availability gradient. *New Phytologist*, *223*(2),
775 632–646. <https://doi.org/10.1111/nph.15684>
- 776 Sánchez-Costa, E., Poyatos, R., & Sabaté, S. (2015). Contrasting growth and water use strategies in four co-
777 occurring Mediterranean tree species revealed by concurrent measurements of sap flow and stem diameter
778 variations. *Agricultural and Forest Meteorology*, *207*, 24–37.
779 <https://doi.org/10.1016/j.agrformet.2015.03.012>
- 780 Schumacher, D. L., Keune, J., van Heerwaarden, C. C., Vilà-Guerau de Arellano, J., Teuling, A. J., & Miralles, D.
781 G. (2019). Amplification of mega-heatwaves through heat torrents fuelled by upwind drought. *Nature*
782 *Geoscience*, *12*(9), 712–717. <https://doi.org/10.1038/s41561-019-0431-6>
- 783 Seneviratne, S. I., Zhang, X., Adnan, M., Badi, W., Dereczynski, C., Di Luca, A., et al. (2021). Weather and Climate
784 Extreme Events in a Changing Climate. In V. Masson-Delmotte, P. Zhai, A. Pirani, S. L. Connors, C. Péan,

- 785 S. Berger, et al. (Eds.), *Climate Change 2021: The Physical Science Basis. Contribution of Working Group*
786 *I to the Sixth Assessment Report of the Intergovernmental Panel on Climate Change* (pp. 1513–1766).
787 Cambridge, United Kingdom and New York, NY, USA: Cambridge University Press.
788 <https://doi.org/10.1017/9781009157896.013>
- 789 Shiflett, S. A., Liang, L. L., Crum, S. M., Feyisa, G. L., Wang, J., & Jenerette, G. D. (2017). Variation in the urban
790 vegetation, surface temperature, air temperature nexus. *Science of the Total Environment*, 579, 495–505.
791 <https://doi.org/10.1016/j.scitotenv.2016.11.069>
- 792 Sousa, P. M., Barriopedro, D., Ramos, A. M., García-Herrera, R., Espírito-Santo, F., & Trigo, R. M. (2019). Saharan
793 air intrusions as a relevant mechanism for Iberian heatwaves: The record breaking events of August 2018
794 and June 2019. *Weather and Climate Extremes*, 26. <https://doi.org/10.1016/j.wace.2019.100224>
- 795 Still, C. J., Rastogi, B., Page, G. F. M., Griffith, D. M., Sibley, A., Schulze, M., et al. (2021). Imaging canopy
796 temperature: shedding (thermal) light on ecosystem processes. *New Phytologist*, 230(5), 1746–1753.
797 <https://doi.org/10.1111/nph.17321>
- 798 Still, C. J., Page, G., Rastogi, B., Griffith, D. M., Aubrecht, D. M., Kim, Y., et al. (2022). No evidence of canopy-
799 scale leaf thermoregulation to cool leaves below air temperature across a range of forest ecosystems.
800 *Proceedings of the National Academy of Sciences*, 119(38), e2205682119.
801 <https://doi.org/10.1073/pnas.2205682119>
- 802 Teuling, A. J., Seneviratne, S. I., Stöckli, R., Reichstein, M., Moors, E., Ciais, P., et al. (2010). Contrasting response
803 of European forest and grassland energy exchange to heatwaves. *Nature Geoscience*, 3(10), 722–727.
804 <https://doi.org/10.1038/ngeo950>
- 805 Wang, P., Li, D., Liao, W., Rigden, A., & Wang, W. (2019). Contrasting Evaporative Responses of Ecosystems to
806 Heatwaves Traced to the Opposing Roles of Vapor Pressure Deficit and Surface Resistance. *Water*
807 *Resources Research*, 55(6), 4550–4563. <https://doi.org/10.1029/2019WR024771>
- 808 te Wierik, S. A., Cammeraat, E. L. H., Gupta, J., & Artzy-Randrup, Y. A. (2021). Reviewing the Impact of Land
809 Use and Land-Use Change on Moisture Recycling and Precipitation Patterns. *Water Resources Research*,
810 57(7). <https://doi.org/10.1029/2020WR029234>
- 811 Williams, I. N., & Torn, M. S. (2015). Vegetation controls on surface heat flux partitioning, and land-atmosphere
812 coupling. *Geophysical Research Letters*, 42(21), 9416–9424. <https://doi.org/10.1002/2015GL066305>

- 813 Xiao, J., Fisher, J. B., Hashimoto, H., Ichii, K., & Parazoo, N. C. (2021). Emerging satellite observations for diurnal
814 cycling of ecosystem processes. *Nature Plants*, 7(7), 877–887. <https://doi.org/10.1038/s41477-021-00952-8>
- 815 Yan, J. W., Liu, J. Y., Chen, B. Z., Feng, M., Fang, S. F., Xu, G., et al. (2014). Changes in the land surface energy
816 budget in eastern China over the past three decades: Contributions of land-cover change and climate
817 change. *Journal of Climate*, 27(24), 9233–9252. <https://doi.org/10.1175/JCLI-D-13-00492.1>
- 818 Yi, K., Smith, J. W., Jablonski, A. D., Tatham, E. A., Scanlon, T. M., Lerdau, M. T., et al. (2020). High
819 Heterogeneity in Canopy Temperature Among Co-occurring Tree Species in a Temperate Forest. *Journal*
820 *of Geophysical Research: Biogeosciences*, 125(12). <https://doi.org/10.1029/2020JG005892>
- 821 Zhang, Q., Barnes, M., Benson, M., Burakowski, E., Oishi, A. C., Ouimette, A., et al. (2020). Reforestation and
822 surface cooling in temperate zones: Mechanisms and implications. *Global Change Biology*, 26(6), 3384–
823 3401. <https://doi.org/10.1111/gcb.15069>
- 824 Zhu, Z., Piao, S., Myneni, R. B., Huang, M., Zeng, Z., Canadell, J. G., et al. (2016). Greening of the Earth and its
825 drivers. *Nature Climate Change*, 6(8), 791–795. <https://doi.org/10.1038/nclimate3004>

826

827

828